

Simple Colloidal Synthesis of Single-Crystal Sb–Se–S Nanotubes with Composition Dependent Band-Gap Energy in the Near-Infrared

Zhengtao Deng,^{*,†‡} Masud Mansuripur,[‡] and Anthony J. Muscat[†]

Department of Chemical and Environmental Engineering and College of Optical Sciences, The University of Arizona, Tucson, Arizona 85721

Received January 27, 2009; Revised Manuscript Received March 16, 2009

ABSTRACT

We report the first synthesis of high-quality binary and ternary $\text{Sb}_2\text{Se}_{3-x}\text{S}_x$ nanotubes across the entire compositional range from $x = 0$ to 3 via a simple, low-cost, colloidal synthetic method of injection of Sb(III)-complex solution into a hot paraffin liquid containing Se, S, or a mixture thereof. In contrast to the classic rolling mechanism, the modular formation of the reported nanotubes follows a four-stage self-seeding process: (i) amorphous nanospheres, (ii) short crystalline nanotubes growing out of relatively large amorphous nanospheres, (iii) long crystalline nanotubes attached to small amorphous nanospheres, and (iv) single-crystal nanotubes. The obtained single-crystal nanotubes have tunable composition, orthorhombic phase, well-defined rectangular cross sections, and growth direction along [001], as revealed by X-ray diffraction, scanning electron microscopy, energy-dispersive X-ray spectroscopy, transmission electron microscopy, and selected area electron diffraction studies. UV–vis–NIR absorption spectroscopy reveals that the optical bandgap energy of the $\text{Sb}_2\text{Se}_{3-x}\text{S}_x$ ($0 \leq x \leq 3$) nanotubes increases quadratically with the sulfur concentration x with these bandgap energies falling in the range from 1.18 to 1.63 eV at the red edge of the solar spectrum. The present study opens a new avenue to low-cost, large-scale synthesis of high quality semiconductor nanotubes with technological applications in solar energy conversion and also for a wide range of optical nanodevices operating in the near-infrared.

Main-group compounds V_2VI_3 ($\text{V} = \text{As, Sb, Bi}$; $\text{VI} = \text{S, Se, Te}$) materials have applications in catalytic agents, thermoelectric devices, optoelectronic devices, and infrared spectroscopy.^{1–3} Among these compounds, Sb_2S_3 and Sb_2Se_3 are important photoconductive semiconductors ($E_g = 1.64$ and 1.11 eV, respectively) that crystallize in the orthorhombic system (pbm space group).^{4–6} Their useful properties (e.g., photovoltaic, photoconducting, photocatalytic, Peltier effect) make them promising candidates for important applications in diverse areas such as solar energy conversion, thermoelectric cooling, photodetector technology, thermoelectric power generation, and opto-electronics in the near-infrared region.^{7,8} Ternary alloys of $\text{Sb}_2\text{Se}_{3-x}\text{S}_x$ ($0 < x < 3$) may have composition-dependent bandgap energies, and due to disorder-induced phonon scattering processes may have lower lattice thermal conductivities and better efficiency in solar energy conversion than the binary compounds.⁹ Inorganic semiconducting hollow nanotubes could be advantageous in nano-scale electronics, optoelectronics, and biochemical sensing

applications. However, synthesis of binary Sb_2Se_3 , Sb_2S_3 , and ternary $\text{Sb}_2\text{Se}_{3-x}\text{S}_x$ ($0 < x < 3$) nanotubes is still difficult for industrial applications; there exist great challenges to obtaining high-quality nanotubes using a simple, inexpensive, and efficient approach. Although various methods have been developed for the fabrication of one-dimensional (1D) Sb_2S_3 and Sb_2Se_3 nanostructures including nanorods, nanowires, and nanoribbons, investigations of nanotube synthesis are quite rare.^{10–13} In 2004, Chen's group reported the synthesis of Sb_2S_3 nanotubes for the first time via the chemical vapor transport reaction.¹⁴ In 2007, Son's group reported the synthesis of Sb_2S_3 nanotubes with ultrathin walls (1.5–2.0 nm) via the rolling mechanism.¹⁵ To our knowledge, no effective techniques have been reported for the synthesis of binary Sb_2Se_3 and ternary $\text{Sb}_2\text{Se}_{3-x}\text{S}_x$ ($0 < x < 3$) nanotubes.

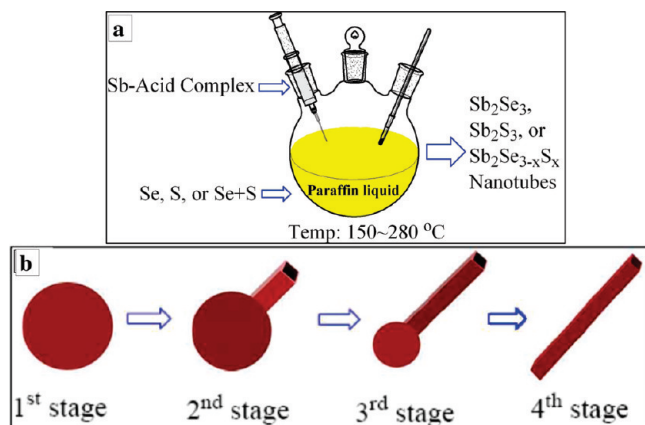
Here we report the synthesis of single-crystal $\text{Sb}_2\text{Se}_{3-x}\text{S}_x$ nanotubes across the entire compositional range from $x = 0$ to 3 by a simple colloidal process involving the injection of Sb(III)-complex solution into a hot Se, S, or their mixture in paraffin liquid. This represents the first synthesis of binary Sb_2Se_3 nanotubes and ternary Sb–Se–S 1D nanostructures. We also discovered that the optical bandgap energy of the as-synthesized $\text{Sb}_2\text{Se}_{3-x}\text{S}_x$ ($0 \leq x \leq 3$) nanotubes increases

* To whom correspondence should be addressed. E-mail: dengz@email.arizona.edu.

[†] Department of Chemical and Environmental Engineering

[‡] College of Optical Sciences

Scheme 1. (a) Overall Synthetic Scheme of Sb_2S_3 , $\text{Sb}_2\text{Se}_{3-x}\text{S}_x$ ($0 < x < 3$), and Sb_2Se_3 Nanotubes; (b) Schematic Illustration of the Proposed Nanotube Formation Mechanism



quadratically with sulfur concentration x , the bandgap energy being finely tunable in the range from 1.18 to 1.63 eV.

As shown in Scheme 1a, the current synthetic method is modeled on the well-developed technique for colloidal synthesis of high-quality CdSe nanocrystals, which involves the injection of trioctylphosphine (TOP)-selenium precursor into the Cd-complex solution at 250–300 °C in a high-boiling-point solvent such as trioctylphosphine oxide (TOPO).^{16–18} Deng et al. modified this classic procedure by using “green” and low-cost paraffin liquid as the solvent, dissolving Se powder in paraffin liquid directly (i.e., without TOP), to synthesize zinc blende CdSe nanocrystals.¹⁹ This technique avoided the use of TOP for dissolving the Se powder, as TOP is a hazardous, unstable, expensive, and environmentally harmful solvent, whereas paraffin liquid [$\text{CH}_3(\text{CH}_2)_n\text{CH}_3$, $n = 16–22$] is a nontoxic, environmentally friendly, inexpensive, and stable solvent with boiling points above 300 °C.^{19–21}

Taking Sb_2Se_3 nanotubes for an example, the synthesis involves the injection of Sb(III)-2-ethylhexanoic acid (EHA) complex into the Se-paraffin liquid solution at the temperature of 220 °C (for the experimental details see Supporting Information). Immediately after injection, the color of the mixed solution turned from yellow to gray black, indicating the formation of Sb_2Se_3 species. Serial aliquots were taken at different intervals for monitoring the kinetics of nanotube formation, and the resulting solid products were purified and imaged with scanning electron microscopy (SEM), as shown in Figure 1a, Figures S1 and S2 (see Supporting Information). In the initial stage, depicted in Figure 1a (5 s), noncrystalline and homogeneous nanospheres with diameters ~ 180 nm were obtained at 5 s reaction; no crystalline nanostructures or nanotubes were observed at this stage, as revealed by the X-ray diffraction (XRD) patterns in Figure 1d. In the second stage, there appeared a small amount of short nanotubes growing on the surface of each nanosphere with crystalline peaks showing up in the XRD pattern at 15 s reaction. By the third stage, relatively long nanotubes had emerged with only a small residue of the original amorphous nanosphere still remaining at 60 s reaction. Finally, in the fourth stage,

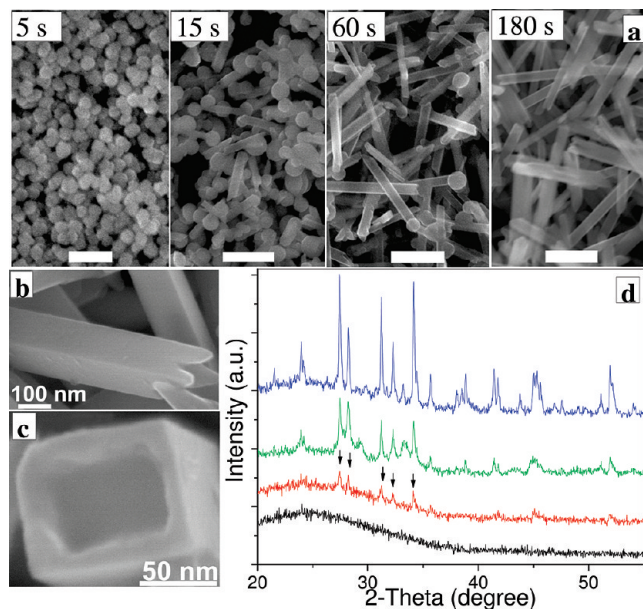


Figure 1. (a) From left to right, representative SEM images of Sb_2Se_3 products harvested at 220 °C after $t = 5, 15, 60,$ and 180 s reaction time; all scale bars are 500 nm; (b,c) enlarged SEM images of typical Sb_2Se_3 nanotubes harvested after $t = 180$ s reaction time; (d) from bottom to top, XRD patterns of the same Sb_2Se_3 samples as in panel a after $t = 5, 15, 60,$ and 180 s reaction time; black arrows in panel d indicate the formation of crystalline species.

there were uniform nanotubes only (i.e., no amorphous spheres) at 180 s reaction. Transmission electron microscopy (TEM) images shown in Figure S3 (see Supporting Information) are consistent with our SEM results. The SEM images in Figure 1a (180 s) and Figure S1 (see Supporting Information) reveal that the end product contains a large quantity of uniform 1D Sb_2Se_3 nanotubes with lengths of $\sim 1 \mu\text{m}$ and diameter of ~ 100 nm. Closer inspection reveals the product to have a hollow cuboidal morphology with a well-defined rectangular cross-section; see Figure 1b,c. Typical nanotubes are ~ 100 nm wide, ~ 80 nm thick, and have wall thickness ~ 10 nm.

On the basis of the above observations, we performed a simple mass calculation to study the transformation process from nanospheres to nanotubes. The volume of a solid nanosphere is given by

$$V = \frac{4\pi}{3} \times \left(\frac{D}{2}\right)^3 \quad (1)$$

Assuming a diameter $D = 180$ nm, the volume of a single nanosphere will be $3.1 \times 10^6 \text{ nm}^3$. For a Sb_2Se_3 nanotube, the volume could be calculated using

$$V = L \times [H \times D - (H - 2d) \times (D - 2d)] \quad (2)$$

Here $L = 1000$ nm, $H = 100$ nm, $D = 80$ nm, and $d = 10$ nm. The volume of a single Sb_2Se_3 nanotube is thus found to be $3.2 \times 10^6 \text{ nm}^3$. Supposing the equal densities for the amorphous Sb_2Se_3 nanospheres and crystalline Sb_2Se_3 nanotubes, the masses of the solid amorphous Sb_2Se_3 nanospheres and hollow crystalline Sb_2Se_3 nanotubes should be nearly identical. Thus, the above simple calculation strongly supports our postulated transformation of a single solid amor-

phous Sb_2Se_3 nanosphere to a single hollow crystalline Sb_2Se_3 nanotube.

In addition, our UV–vis–NIR absorption spectra obtained as function of reaction time show that the absorption onset does not shift much (~ 0.05 eV) during the transformation process from amorphous nanosphere to single-crystal nanotubes as shown in Figure S2f,g (see Supporting Information), whereas the XRD patterns obtained after different reaction times show the increasing crystallinity of the product (see Figure 1d).

The above results clearly indicate that the formation of nanotubes follows a four-stage, self-seeding process as shown in Scheme 1b: (i) formation of amorphous nanospheres that act as sacrificial reservoirs for Sb_2Se_3 nanotubes; (ii) growth of short nanotubes out of relatively large nanospheres; (iii) long nanotubes attached to small residual nanospheres; and (iv) complete nanotubes with no nanospheres attached. To further verify the growth mechanism, we performed the control experiment with double precursor Sb(III) and Se concentrations, while keeping the other experimental parameters as the same. As shown in Figure S4 (see Supporting Information), the TEM images of the Sb_2Se_3 products harvested at different intervals demonstrated that the larger sized nanotubes (~ 250 nm in diameter, ~ 5 μm in length) were grown from larger sized nanospheres (~ 700 nm in diameter); the well-defined four-stage self-seeding growth process is consistent with the observations from the lower precursor concentrations. It is expected that the sizes of the nanotubes could be further tuned by changing the reaction parameters such as the concentration of the precursors and reaction temperature. We believe that the formation of Sb_2Se_3 nanotubes was via the preferential formation of the crystalline Sb_2Se_3 species on the surface of the amorphous nanospheres. As soon as the crystalline species were grown, mass transport to the growing region in one end of the nanotubes would lead to depletion of the amorphous nanospheres as the sacrificial reservoirs in another end and eventually resulted in the formation of the well-defined nanotubes.

In somewhat similar fashion, Xia's group has demonstrated the synthesis of Te nanotubes by directly nucleating and growing from aqueous orthotelluric acid solution.²² In their growth mechanism, Te nanotubes could be preferentially grown at the circumferential edges of the crystalline cylindrical Te solid seeds via control the concentration of the Te in bulk solution. Then, the mass transport to the growing regions would lead to depletion of the Te in the center cylindrical solid seeds and result in the formation of the nanotubes with hollow interiors.²² Also, Ding's group has demonstrated the formation of TiO_2 nanotubes through CeO_2 colloid-seeded deposition process in solution.²³ Contrastively, there is a classic rolling mechanism for the growth of inorganic nanotubes, which was derived from the successful synthesis of nanotubes of carbon and other inorganic materials with layered structures in their bulk crystals.²⁴ Nevertheless, our synthetic technique demonstrates the first formation of V_2VI_3 nanotubes through a self-seeding process in solution. Our synthetic method is modular, and we have extended it to

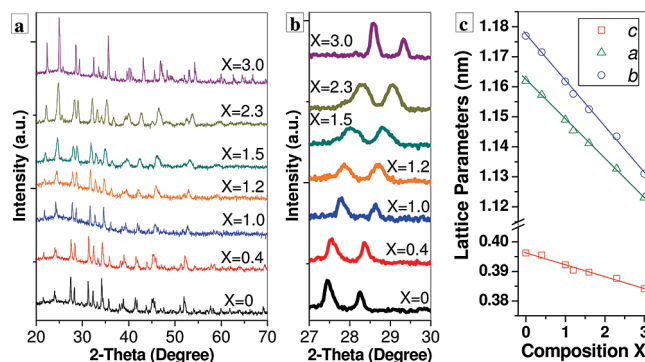


Figure 2. (a) From bottom to top, XRD patterns of the $\text{Sb}_2\text{Se}_{3-x}\text{S}_x$ ($0 \leq x \leq 3$) nanotubes with their precursor sulfur concentration x indicated; (b) (230) and (211) XRD peaks of the same nanotubes as in panel a; (c) lattice constants a (green), b (blue), and c (red), derived from XRD diffraction peaks and HRTEM images, plotted as functions of precursor sulfur concentration x .

the synthesis of single-crystal Sb_2S_3 and $\text{Sb}_2\text{Se}_{3-x}\text{S}_x$ ($0 < x < 3$) nanotubes with rectangular cross-section.

Figure 2a and Figure S5 (see Supporting Information) show the X-ray diffraction (XRD) patterns of seven different $\text{Sb}_2\text{Se}_{3-x}\text{S}_x$ ($0 \leq x \leq 3$) nanotubes with their precursor sulfur concentration x of 0, 0.4, 1.0, 1.2, 1.5, 2.3, and 3.0 respectively; the observed features are in good agreement with those of the typical orthorhombic crystals. It is clearly seen that the diffraction peaks from Sb_2Se_3 , $\text{Sb}_2\text{Se}_{2.6}\text{S}_{0.4}$, $\text{Sb}_2\text{Se}_{2.0}\text{S}_{1.0}$, $\text{Sb}_2\text{Se}_{1.8}\text{S}_{1.2}$, $\text{Sb}_2\text{Se}_{1.5}\text{S}_{1.5}$, $\text{Sb}_2\text{Se}_{0.7}\text{S}_{2.3}$, and Sb_2S_3 shift gradually toward larger angles, indicating the decreasing lattice constants of the nanotubes with gradual substitution of the Se atoms with the smaller and lighter S atoms.²⁵ In addition, in none of our samples were any peaks corresponding to other phases detected, indicating that these samples are single-phase. The absence of multiple sets of peaks indicates that the nanotubes are not phase separated.

Figure 2b shows XRD patterns of nanotubes along the compositional gradient. The contraction of the cell is shown in Figure 2b from shifts of the position of the (230) reflection from 27.44, 27.53, 27.77, 27.86, 28.04, 28.31, to 28.58°. According to Vegard's law,²⁶ the lattice parameters have a linear dependence on the composition x ,

$$c(x) = \frac{x}{3} \times c(\text{Sb}_2\text{S}_3) + \left(\frac{3-x}{3}\right) \times c(\text{Sb}_2\text{Se}_3) \quad (3)$$

where $c(\text{Sb}_2\text{Se}_3)$, $c(\text{Sb}_2\text{S}_3)$, and $c(x)$ are the respective c -axis lattice constants of the orthorhombic structured samples. As shown in Figure 2c, the composition x of the nanotubes were determined from Vegard's law using the lattice parameters deduced from the XRD data,^{27–29} which is in good agreement with the precursor sulfur concentration added in the reaction system. Figure 2c shows the lattice constants a , b , and c , determined from XRD, plotted as functions of the sulfur concentration x . The green, blue, and red lines show the Vegard-law approximation of the a , b , and c lattice constants as a function of sulfur concentration using the values of $a = 1.123$ and 1.162 nm, $b = 1.131$ and 1.177 nm, and $c = 0.3841$ and 0.3962 nm for bulk orthorhombic Sb_2S_3 (JCPDS Card No. 42-1393) and bulk orthorhombic Sb_2Se_3 (JCPDS Card No. 72-1184), respectively. This plot shows a near-linear relationship between lattice spacing and alloy com-

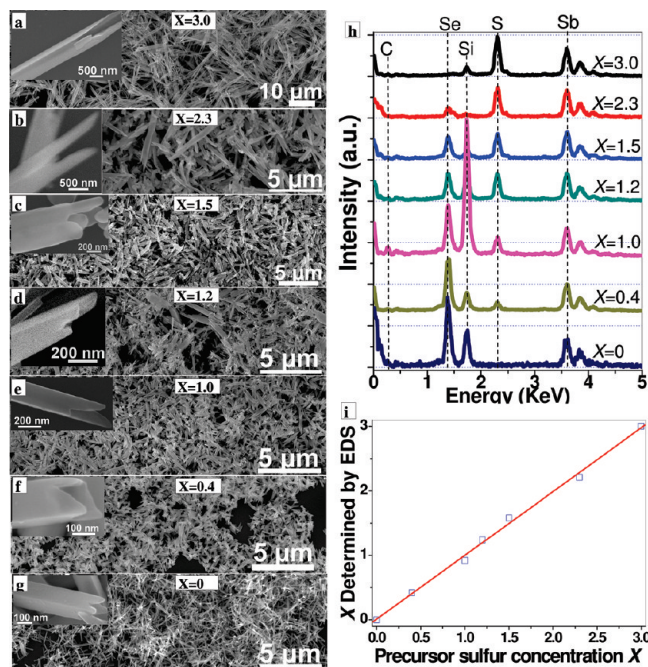


Figure 3. (a–g) SEM images of $\text{Sb}_2\text{Se}_{3-x}\text{S}_x$ ($0 \leq x \leq 3$) nanotubes marked with their precursor sulfur concentration x of 3.0, 2.3, 1.5, 1.2, 1.0, 0.4, and 0, respectively, (a,b,c) samples harvested at 200 °C, (d,e,f,g) samples harvested at 220 °C, insets show the enlarged images of the corresponding single nanotubes; (h) EDS patterns of $\text{Sb}_2\text{Se}_{3-x}\text{S}_x$ ($0 \leq x \leq 3$) nanotubes (normalized with the Sb peak intensity), the Si signals are from the silicon substrate, while the C signals are possibly from the trace organic materials such as paraffin liquid, 2-ethylhexanoic acid, or oleylamine; (i) sulfur concentration x measured directly from the EDS spectra plotted versus the nominal precursor sulfur concentration x .

position. The above results indicate that alloyed $\text{Sb}_2\text{Se}_{3-x}\text{S}_x$ nanotubes with modulated compositions between Sb_2Se_3 and Sb_2S_3 could be obtained during this simple colloidal synthesis process.

The scanning electron microscopy (SEM) images and energy-dispersive X-ray spectroscopy (EDS) patterns in Figure 3, Figures S1, S6, and S7 (see Supporting Information) reveal that the end product contains a large quantity of Sb_2Se_3 , $\text{Sb}_2\text{Se}_{2.6}\text{S}_{0.4}$, $\text{Sb}_2\text{Se}_{2.0}\text{S}_{1.0}$, $\text{Sb}_2\text{Se}_{1.8}\text{S}_{1.2}$, $\text{Sb}_2\text{Se}_{1.5}\text{S}_{1.5}$, $\text{Sb}_2\text{Se}_{0.7}\text{S}_{2.3}$, and Sb_2S_3 nanotubes, respectively. The high magnification SEM images shown in the insets indicate that the nanotubes have diameters varying from 100 to 500 nm, and lengths varying from a few to tens of micrometers. Closer inspection reveals that the products have a hollow cuboidal morphology with a well-defined rectangular cross-section. For example, the SEM images of Sb_2S_3 nanotubes in Figure S6 (see Supporting Information) indicate that the product contains a large quantity of uniform rectangular cross-sectioned nanotubes with $\sim 15 \mu\text{m}$ length, $\sim 400 \text{ nm}$ wide, $\sim 300 \text{ nm}$ thick, and $\sim 20 \text{ nm}$ wall thickness. This well-defined rectangular cross-section morphology of the 1D structure originates from the unit cell of the orthorhombic crystals of V_2VI_3 compounds, similar to the reported Sb_2O_3 nanowires.³⁰ The EDS spectra showed of Figure 3h exhibit only Sb, Se, and/or S peaks, suggesting that the product exclusively contains Sb, Se, and/or S. A quantitative EDS analysis revealed that the measured composition x for each

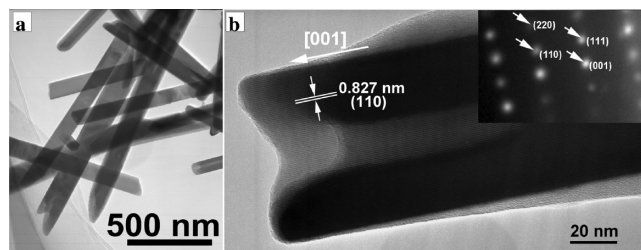


Figure 4. (a) Low-magnification TEM image of the Sb_2Se_3 nanotubes; (b) HRTEM image of one end of a typical Sb_2Se_3 nanotube, revealing a hollowing structure of the product; (inset b) SAED pattern of the Sb_2Se_3 nanotube shown in (b).

samples is 3.0, 2.21, 1.58, 1.24, 0.92, 0.42, and 0. As shown in Figure 3i, the sulfur concentration obtained with a scanning electron microscope by EDS is very close to the results obtained from the XRD patterns, further confirming the composition of the as-synthesized product as $\text{Sb}_2\text{Se}_{3-x}\text{S}_x$ ($0 \leq x \leq 3$), respectively.

The morphologies of the as-synthesized nanotubes were further investigated by TEM. Figure 4a shows the TEM image of the typical 1D product with the width about 100 nm and a length up to $1 \mu\text{m}$. The microstructure of an individual Sb_2Se_3 nanotube shown in Figure 4b reveals the well-defined hollowing nanotube structure feature, consistent with the structural information gleaned from SEM images. The obvious lattice spacings of about 0.827 nm corresponds to (110) planes spacings of orthorhombic phase Sb_2Se_3 (JCPDS Card No. 72-1184). The selected area electron diffraction (SAED) pattern (inset Figure 4b) is a spot pattern, revealing that the nanotube is a single crystal. In addition, the SAED pattern indicated that the nanotube grows along the [001] direction as marked with an arrow shown in Figure 4b. Figure 4 shows that the obtained nanotubes are of high quality and free from dislocation and stacking faults.

As seen in Figure 5, the high-resolution TEM (HRTEM) images of a series of individual nanotubes show the typical (110) spacings of the Sb_2Se_3 , $\text{Sb}_2\text{Se}_{2.6}\text{S}_{0.4}$, $\text{Sb}_2\text{Se}_{2.0}\text{S}_{1.0}$, $\text{Sb}_2\text{Se}_{1.8}\text{S}_{1.2}$, $\text{Sb}_2\text{Se}_{1.5}\text{S}_{1.5}$, $\text{Sb}_2\text{Se}_{0.7}\text{S}_{2.3}$, and Sb_2S_3 samples to be 0.828, 0.823, 0.816, 0.814, 0.811, 0.802, and 0.795 nm, respectively. The indexed fast Fourier transforms (FFTs) of the HRTEM images in Figure 5 clearly indicate a linear decline in the lattice constants of the $\text{Sb}_2\text{Se}_{3-x}\text{S}_x$ alloys with an increasing S concentration, consistent with our XRD results. As shown in Figure S8 (see Supporting Information), the HRTEM image of single $\text{Sb}_2\text{Se}_{2.6}\text{S}_{0.4}$ nanotube indicates that the typical lattice spacings are about 0.804 and 0.387 nm, corresponding to (110) and (001) planes spacings of orthorhombic phase, respectively. The HRTEM image also demonstrates that the nanotubes grows along the [001] direction as indicated with an arrow. These results revealed that all the nanotubes are of high quality.

Analysis of optical absorption spectra is one of the most effective tools for understanding and/or engineering the band structure and energy gaps of semiconductor materials. The optical absorption experiments reported in Figure 6a were carried out to determine the band gap energies of our nanotube samples. For direct band gap semiconductors, the

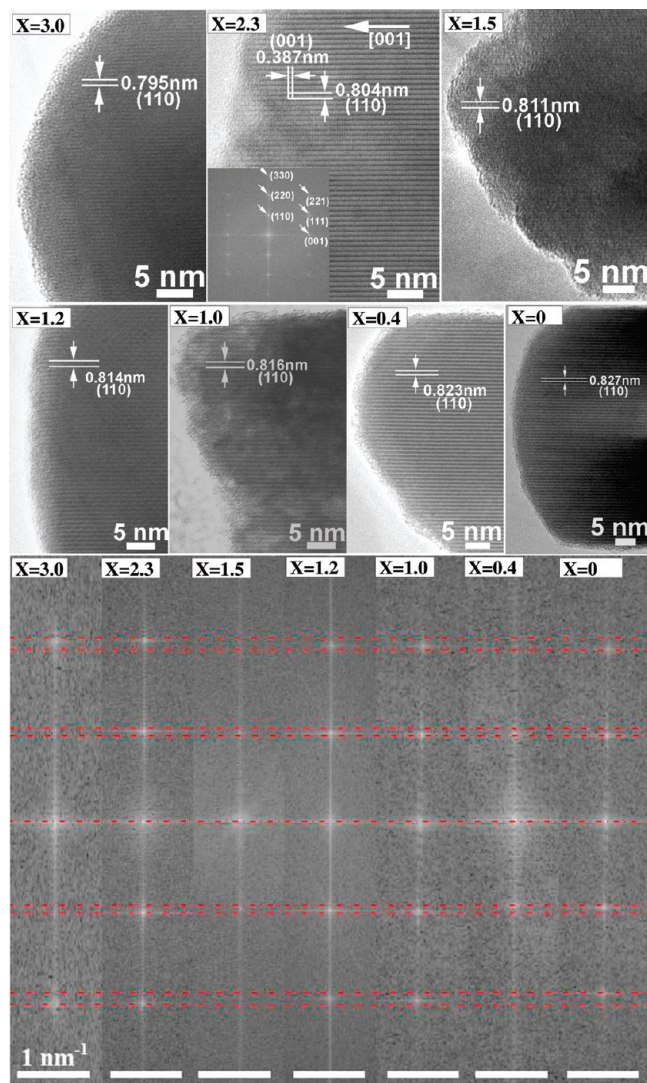


Figure 5. HRTEM images and their indexed fast Fourier transforms (FFTs) of $\text{Sb}_2\text{Se}_{3-x}\text{S}_x$ ($0 \leq x \leq 3$) nanotubes, labeled with the corresponding precursor sulfur concentration x . All scale bars are 1 nm^{-1} .

optical absorption near the band edge follows the formula: $\alpha h\nu = A(h\nu - E_g)^{1/2}$, where α , ν , and E_g are the absorption coefficient, optical frequency, and band gap energy, respectively, while A is a constant.^{6,9} The E_g can thus be estimated from a plot of $(\alpha h\nu)^2$ versus the photon energy ($h\nu$). The estimated band gaps for our various samples were found to be $E_g = 1.63, 1.48, 1.33, 1.29, 1.25, 1.21$, and 1.18 eV ; see Figure 6b. The band gap E_g is thus seen to increase from 1.18 eV for Sb_2Se_3 to 1.63 eV for Sb_2S_3 as the concentration of S increases in the $\text{Sb}_2\text{Se}_{3-x}\text{S}_x$ series.

The dependence of the optical transition energy on composition (x) was found to fit a quadratic equation as shown in Figure 6c and characterized by the following relation

$$E_g(x) = 0.0344x^2 + 0.0481x + 1.18 \text{ eV} \quad (4)$$

The fitted values of the bandgap energy obtained in our measurements are in good agreement with the previously reported values from 1D Sb_2S_3 and Sb_2Se_3 nanostruc-

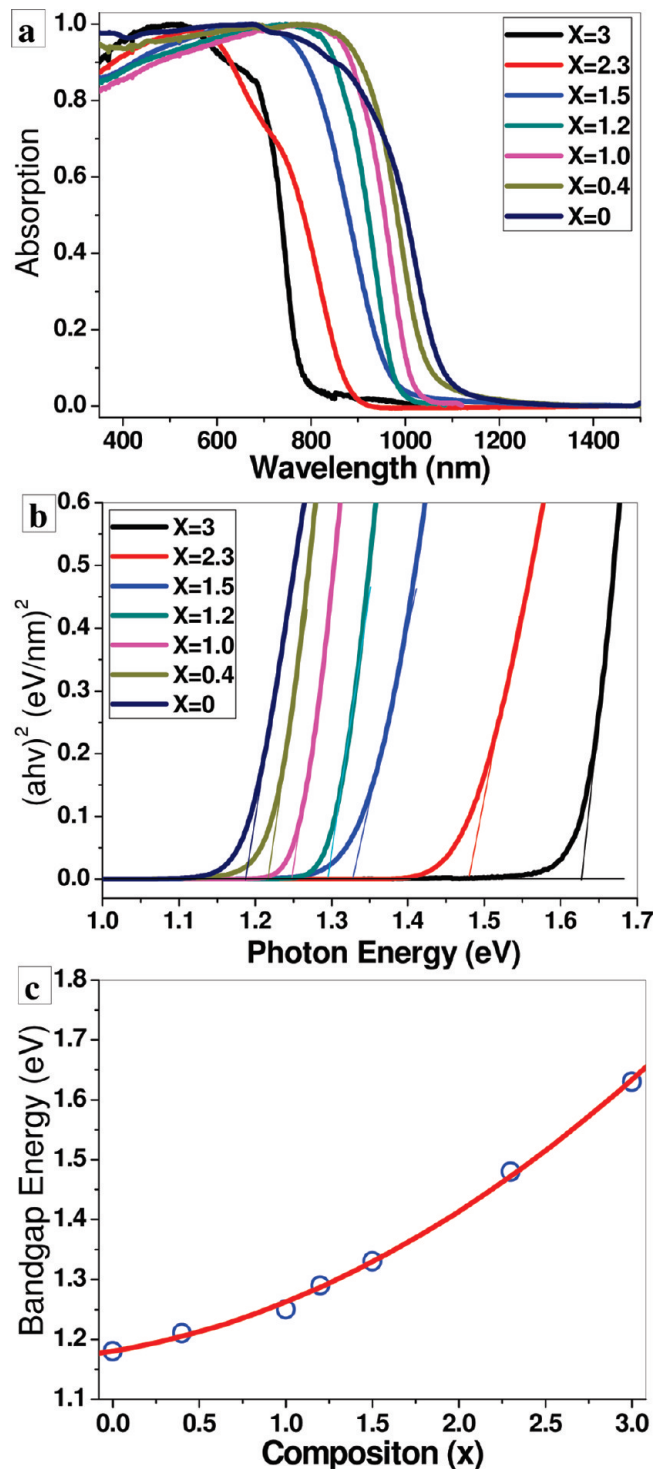


Figure 6. (a) UV-vis-NIR absorption spectra of $\text{Sb}_2\text{Se}_{3-x}\text{S}_x$ ($0 \leq x \leq 3$) nanotubes at room temperature. (b) Plots of $(\alpha h\nu)^2$ vs. the photon energy ($h\nu$) reveal the band-gaps of $\text{Sb}_2\text{Se}_{3-x}\text{S}_x$ nanotube samples as $1.63, 1.48, 1.33, 1.29, 1.25, 1.21$, and 1.18 eV for $x = 3.0, 2.3, 1.5, 1.2, 1.0, 0.4$, and 0 , respectively. (c) The band gap energy plotted versus the sulfur concentration x (nominal precursor sulfur concentration x); the solid curve is a quadratic fit to the measured values of the band gap energy extracted from the absorption spectra in panel b.

tures.^{10–13} Recent reports of thermally evaporated amorphous thin films of $\text{Sb}_2\text{Se}_{3-x}\text{S}_x$ ($x = 0, 1, 2$, and 3) solid solutions indicate a quadratically increasing optical band gap energy with sulfur content, which is in agreement with our findings.⁹

The experimental values of nanotube bandgaps are near the optimum value for photovoltaic conversion, suggesting that these nanotubes may be promising for applications in solar energy and for a wide range of optical nanodevices operating in the near-infrared range. Further work to explore their structures, optical properties, and technological applications is currently underway.

Conclusions. Using a simple and low-cost colloidal synthetic technique involving the injection of Sb(III)-complex source solution into a hot paraffin liquid containing Se, S, or a mixture thereof, we have demonstrated the capability of tuning the composition and the energy gap of single-crystal binary and ternary $\text{Sb}_2\text{Se}_{3-x}\text{S}_x$ ($0 \leq x \leq 3$) nanotubes having rectangular cross sections across the entire composition range. The modular formation of these nanotubes follows a four-stage self-seeding process: (i) amorphous nanospheres, (ii) short crystalline nanotubes growing out of relatively large amorphous nanospheres, (iii) long crystalline nanotubes attached to small amorphous nanospheres, and (iv) single-crystal nanotubes. We have demonstrated the smooth dependence of the bandgap on composition from Sb_2Se_3 to Sb_2S_3 in the near-infrared region from 1.18 to 1.63 eV. The estimated band-gaps of our nanotubes are at the red edge of the solar spectrum, thus suggesting that these nanotubes may hold promise for solar energy conversion as well as for novel opto-electronics applications. By the suitable choice of sources and/or synthetic parameters, it is reasonable to expect that the present methods can be extended to the synthesis of other semiconductor nanotubes as well.

Acknowledgment. We are grateful to Mr. Philip Anderson and Professor Supapan Seraphin of the University Spectroscopy and Imaging Facilities (USIF) at The University of Arizona for help in accessing to the characterization facilities. This work has been supported by the Strategic Research Group Program of Arizona's Science Foundation.

Supporting Information Available: Additional synthesis and characterization details, SEM and TEM images, EDS patterns, UV-vis-NIR absorption spectra, size distribution histograms, and XRD patterns of the samples. This material is available free of charge via the Internet at <http://pubs.acs.org>.

References

- (1) Tritt, T. M. *Science* **1999**, 283, 804.
- (2) Venkantasubramanian, R.; Siilvola, E.; Colpitts, T.; O'Quinn, B. *Nature* **2001**, 413, 597.
- (3) Konstantatos, G.; Levina, L.; Tang, J.; Sargent, E. H. *Nano Lett.* **2008**, 8, 4002.
- (4) Madelung, O.; Schulz, M.; Weiss, H. *Landolt-Börnstein - Group III Condensed Matter Numerical Data and Functional Relationships in Science and Technology*; Springer-Verlag: Berlin, 1998; Vols III/17E-17F-41C.
- (5) Zheng, X. W.; Xie, Y.; Zhu, L. Y.; Jiang, X. C.; Jia, Y. B.; Song, W. H.; Sun, Y. P. *Inorg. Chem.* **2002**, 41, 455.
- (6) Yu, Y.; Wang, R. H.; Chen, Q.; Peng, L. M. *J. Phys. Chem. B* **2006**, 110, 13415.
- (7) Rajapure, K.; Lokhande, C.; Bhosele, C. *Thin Solid Films* **1997**, 311, 114.
- (8) Kim, I. *Mater. Lett.* **2000**, 43, 221.
- (9) El-Sayad, E. A. *J. Non-Cryst. Solids* **2008**, 354, 3806.
- (10) Yu, Y.; Wang, R. H.; Chen, Q.; Peng, L. M. *J. Phys. Chem. B* **2005**, 109, 23312.
- (11) Ota, J.; Srivastava, S. K. *Cryst. Growth Des.* **2007**, 7, 343.
- (12) Chang, H. W.; Sarkar, B.; Liu, C. W. *Cryst. Growth Des.* **2007**, 7, 2691.
- (13) Chen, G. Y.; Deng, B.; Cai, G. B.; Zhang, T.-K.; Dong, W. F.; Zhang, W. X.; Xu, A. W. *J. Phys. Chem. C* **2008**, 112, 672.
- (14) Yang, J.; Liu, Y. C.; Lin, H. M.; Chen, C. C. *Adv. Mater.* **2004**, 16, 713.
- (15) Park, K. H.; Choi, J.; Kim, H.; Jin, J.; Lee, B.; Son, S. U. *Chem. Mater.* **2007**, 19, 3861.
- (16) Murray, C. B.; Norris, D. J.; Bawendi, M. G. *J. Am. Chem. Soc.* **1993**, 115, 8706.
- (17) Peng, Z. A.; Peng, X. G. *J. Am. Chem. Soc.* **2001**, 123, 183.
- (18) Qu, L.; Peng, A.; Peng, X. G. *Nano Lett.* **2001**, 1, 333.
- (19) Deng, Z. T.; Cao, L.; Tang, F. Q.; Zou, B. S. *J. Phys. Chem. B* **2005**, 109, 16671.
- (20) Dahl, J. A.; Maddux, B. L. S.; Hutchison, J. E. *Chem. Rev.* **2007**, 107, 2228.
- (21) Yordanov, G. G.; Yoshimura, H.; Dushkin, C. D. *Colloid Polym. Sci.* **2008**, 286, 813.
- (22) Mayers, B.; Xia, Y. *Adv. Mater.* **2002**, 14, 279.
- (23) Lin, Y.; Gao, W.; Zhang, D. Y.; Guo, X. F.; Ding, W. P.; Chen, Y. *J. Am. Chem. Soc.* **2006**, 128, 11042.
- (24) Li, Y. D.; Wang, J. W.; Deng, Z. X.; Wu, Y. Y.; Sun, X. M.; Yu, D. P.; Yang, P. D. *J. Am. Chem. Soc.* **2001**, 123, 9904.
- (25) Malliakas, C. D.; Kanatzidis, M. G. *J. Am. Chem. Soc.* **2006**, 128, 6538.
- (26) Vegard, L.; Schjelderup, H. Z. *Phys.* **1917**, 18, 93.
- (27) Deng, Z. T.; Lie, F. L.; Shen, S. Y.; Ghosh, I.; Mansuripur, M.; Muscat, A. J. *Langmuir* **2009**, 25, 434.
- (28) Pan, A.; Yang, H.; Liu, R.; Yu, R.; Zou, B.; Wang, Z. L. *J. Am. Chem. Soc.* **2005**, 127, 15692.
- (29) Kuykendall, T.; Ulrich, P.; Aloni, S.; Yang, P. *Nat. Mater.* **2007**, 6, 951.
- (30) Deng, Z. T.; Tang, F. Q.; Chen, D.; Meng, X. W.; Cao, L.; Zou, B. S. *J. Phys. Chem. B* **2006**, 110, 18225.

NL9002816